Compositional data analysis of Holocene sediments from the West Bengal Sundarbans, India: Geochemical proxies for grain-size variability in a delta environment

Accepted Manuscript

Compositional data analysis of Holocene sediments from the West Bengal Sundarbans, India: Geochemical proxies for grain-size variability in a delta environment

R.P. Flood, M.R. Bloemsma, G.J. Weltje, I.D. Barr, S.M. O'Rourke, J.N. Turner, J.D. Orford

PII: S0883-2927(16)30114-7

DOI: 10.1016/j.apgeochem.2016.06.006

Reference: AG 3673

To appear in: *Applied Geochemistry*

Received Date: 5 November 2015

Revised Date: 13 June 2016

Accepted Date: 22 June 2016

Please cite this article as: Flood, R.P., Bloemsma, M.R., Weltje, G.J., Barr, I.D., O'Rourke, S.M., Turner, J.N., Orford, J.D., Compositional data analysis of Holocene sediments from the West Bengal Sundarbans, India: Geochemical proxies for grain-size variability in a delta environment, *Applied Geochemistry* (2016), doi: 10.1016/j.apgeochem.2016.06.006.

Compositional data analysis of Holocene sediments from the West Bengal Sundarbans, India: geochemical proxies for grain-size variability in a delta environment

R.P. Flood[1,2*], M.R. Bloemsma[3], G.J. Weltje[4], I.D. Barr[1], S.M. O'Rourke[5], J.N. Turner[6], J.D. Orford[1]

[1]School of Geography, Archaeology, and Palaeoecology, Queen's University Belfast, BT7 1NN, Northern Ireland, UK

[2]Present address: School of Natural Sciences, Trinity College Dublin, Dublin 2, Republic of Ireland

[3]Tata Steel - Netherlands Main Office, Postbus 10000, 1970 CA Ijmuiden, The Netherlands

[4]Department of Earth and Environmental Sciences, Geology Division, University of Leuven, Celestijnenlaan 200E, 3001 Leuven-Heverlee, Belgium

[5]School of Biosystems Engineering, University College Dublin, Belfield, Dublin 4, Republic of Ireland

[6]School of Geography & UCD Earth Institute, University College Dublin, Belfield, Dublin 4, Republic of Ireland

[*]Corresponding author. Email Address: rpflood@tcd.ie Phone number: +35318962661

Keywords: compositional data; Ganges-Brahmaputra delta; XRF; calibration; geochemistry; grain-size; partial least squares.

ABSTRACT

This paper is part of a special issue of Applied Geochemistry focusing on reliable applications of compositional multivariate statistical methods. This study outlines the application of compositional data analysis (CoDa) to calibration of geochemical data and multivariate statistical modelling of geochemistry and grain-size data from a set of Holocene sedimentary cores from the Ganges-Brahmaputra (G-B) delta. Over the last two decades, understanding near-continuous records of sedimentary sequences has required the use of core-scanning X-ray fluorescence (XRF) spectrometry, for both terrestrial and marine sedimentary sequences. Initial XRF data are generally unusable in 'raw-format', requiring data processing in order to remove instrument bias, as well as informed sequence interpretation. The applicability of these conventional calibration equations to core-scanning XRF data are further limited by the constraints posed by unknown measurement geometry and specimen homogeneity, as well as matrix effects. Log-ratio based calibration schemes have been developed and applied to clastic sedimentary sequences focusing mainly on energy dispersive-XRF (ED-XRF) core-scanning. This study has applied high resolution core-scanning XRF to Holocene sedimentary sequences from the tidal-dominated Indian Sundarbans, (Ganges-Brahmaputra delta plain). The Log-Ratio Calibration Equation (LRCE) was applied to a sub-set of core-scan and conventional ED-XRF data to quantify elemental composition. This provides a robust calibration scheme using reduced major axis regression of log-ratio transformed geochemical data. Through partial least squares (PLS) modelling of geochemical and grain-size data, it is possible to derive robust proxy information for the Sundarbans depositional environment. The application of these techniques to Holocene sedimentary

47 data offers an improved methodological framework for unravelling Holocene
48 sedimentation patterns.
49
50 **1. GEOCHEMISTRY OF HOLOCENE SEDIMENTARY ENVIRONMENTS**
51 The composition and physical properties of sediments and sedimentary rocks are for the
52 most part controlled by chemical processes taking place during weathering, transport, and
53 burial (diagenesis) (Bjørlykke, 2010). Thus, understanding the physical properties of
54 sediments and sedimentary rocks requires an understanding of the chemical processes
55 underlying sedimentary deposition. The formation of clastic sediments is a result of the
56 erosion and weathering of source parent rocks. The dissolved fraction of this clastic
57 sediment flows into seas or lakes, with subsequent precipitation as biological or chemical
58 sediments. During transport, grains continue to undergo weathering and abrasion, with
59 resultant sediments potentially undergoing repeated cycles of deposition and erosion prior
60 to final deposition. In order to establish the origin of these sediments, and to gain an
61 understanding of the processes that have operated prior to their deposition, there is a need
62 to analyse their geochemistry. For Holocene sediments (i.e., those deposited within the
63 last 11.7 ka), environmental geochemistry offers a series of approaches to analyse
64 sediment geochemistry. For example, the identification of minerals in soils and sediments
65 usually involves high powered electron microscopy to image crystal forms, and
66 diffraction and vibrational spectroscopy to determine crystallographic structures (Ryan,
67 2014). Understanding the elemental composition of sediment usually involves the
68 analysis of elemental absorbance, emission, fluorescence or mass (Ryan, 2014). These
69 approaches to elemental analysis fall into two groups: destructive and non-destructive.

The former involve the dissolution of minerals into an aqueous solution, whilst the latter are characterised by the analysis of mineral powders (Ryan, 2014). These non-destructive approaches include X-ray fluorescence (XRF) which this study will examine for the purposes of the chemometric calibration of element geochemistry from the Sundarbans, West Bengal, India. This paper provides a background to XRF, XRF core-scanning and calibration through compositional data analysis (CoDa), with a focus on the sediments of the Sundarbans, to demonstrate the usefulness of the techniques. Through the application of CoDa, a number of calibration coefficients can be derived for key proxy geochemical indicators and used to study sedimentary provenance and depositional processes. The objective of the study is to investigate how the application of LRCE & PLS to Holocene sediments of a Delta environment can improve interpretation of geochemical indicators of grain-size variability.

2. BACKGROUND TO THE INDIAN SUNDARBANS

The Sundarbans is one of the largest coastal wetland sites in the world (~ 1 million hectares) covering the western delta of the Ganges and Brahmaputra (G-B) rivers (Fig. 1). The Sundarbans is a complex network of tidal creeks and deltaic islands with most sediment arriving indirectly from the G-B river systems (which drain the Himalayas). The Indian Sundarbans comprises just over 400,000 hectares in the western sector of the G-B delta, and is cross-cut by a number of approximately north-south estuarine channels (Fig. 2). Overall, the G-B delta is generally divided into two sub-systems of fluvially and non-fluvially dominated depositional environments (Fig. 1) (Rogers et al., 2013). The eastern sector of G-B delta comprises the fluvially dominated system, whilst the older

93 abandoned part of the delta, in the west, comprises the non-fluvially dominated
94 environment that is no longer directly linked to the G-B river sources (Fig. 1). This
95 western part of the delta (which underlies the present day Indian Sundarbans) was
96 fluvially abandoned prior to c. 5000 cal yr BP, as the Ganges River migrated eastward
97 towards its present position (Goodbred and Kuehl, 2000). Shoreline progradation in the
98 eastern delta complex following the joining of the Ganges and Brahmaputra rivers in the
99 Meghna Estuary is considered to be fluvially-dominated (Allison, 1998a).

100 The western extent of the G-B delta is now thought to be undergoing net delta
101 front erosion (Allison, 1998b; Allison et al., 2003), likely reflecting an eroding
102 environment in areas distal to areas of contemporary fluvial-deltaic deposition (Allison
103 (1998b). As the Ganges river shifted from its former western discharge channel (i.e.,
104 Hoogly River) to its current position in the east, a series of palaeo-distributary channels
105 were left abandoned (Allison, 1998b). These channels reflect an almost exclusively tidal-
106 driven geomorphology, with sediments and discharge from the main G-B rivers no longer
107 entering the western delta front (Allison, 1998b; Bhattacharyya et al., 2013).

108 In order to fully explore the processes of sedimentation and the potential sources
109 of variance in sediment composition during the late-Holocene (post Ganges shift), high
110 resolution data analysis is required. Such analysis has never been performed on
111 sedimentary cores from the Sundarbans, and this study represents the first attempt at
112 characterising the sedimentary facies using high-resolution core-scan XRF and
113 establishing variation in sediment deposition.

114

115 **3. INTRODUCTION TO XRF CORE-SCANNING**

The application of X-ray fluorescence (XRF) to geological materials is well established, and recognised as a conventional technique for deriving elemental composition (Ramsey et al., 1995; Jenkins, 1999; De Vries and Vrebos, 2002; Weltje and Tjallingii, 2008). The underlying principle of XRF analysis is that excitation of electrons by incident X-radiation (X-rays) leads to the ejection of electrons from the inner ring of an atomic shell. This ejection results in a vacancy, which is filled by cascading electrons from the outer shells, which, in turn, leads to the emission of energy (Weltje and Tjallingii, 2008). The emitted energy and wavelength spectra are atomically indicative of particular elements, allowing relative abundances of elemental compositions to be derived (Weltje and Tjallingii, 2008).

In the 1990s, the development of a non-destructive core logging technique which applies XRF for the determination of major-element concentrations in split sediment cores was first utilised by the Royal Netherlands Institute for Sea Research (NIOZ) (Jansen et al., 1998). The most advantageous surface for XRF sample determination is homogeneous, dry, and smooth (Jansen et al., 1998). Using split-cores surfaces provides comparable geochemical data to powder samples (Jensen et al., 1998). This is due to the response depths that vary between elements. However, it has been found problematic that larger particles tend to attenuate the fluorescent radiation of elements more than fine particles (Jansen et al., 1998). The ‘ideal’ homogeneity of a sample occurs when the majority of the material can pass through a 70-mm sieve (Potts, 1987; Jansen et al., 1998), with ‘ideal’ results derived from silts and clays, rather than from sands (which require careful interpretation of results) (Jansen et al., 1998). The key advantages of XRF core-scanning over conventional geochemical analysis of discrete specimens is that

element intensities are obtained directly at the surface of a split sediment core (allowing for the extraction of near-continuous records of element intensities), and the spatial resolution of ED-XRF core-scanning is much higher than conventional discrete sampling destructive methods (Weltje and Tjallingii, 2008). However, one of the main drawbacks of the approach has been the conversion of element intensities measured by ED-XRF core-scanners to element concentrations (Weltje and Tjallingii, 2008). Thus, the results obtained by ED-XRF core-scanning are generally presented in the form of count rates (counts per unit time per unit area), or as ratios of counts, count rates, or intensities of elements (Richter et al., 2006; Rothwell et al., 2006; Thomson et al., 2006; Weltje and Tjallingii, 2008). Within regular calibration schemes, measurement geometry and specimen homogeneity is very poorly constrained due to the inhomogeneity of samples and the irregular surface of a split-core (Weltje and Tjallingii, 2008; Weltje et al., 2015). In addition, in some instances, spatial variations in the thickness of an adhesive pore-water film which forms directly below a protective polyester film covering the split core surface should be considered a further constraining factor on measurement geometry values in the calibration equation (Weltje and Tjallingii, 2008). Due to these poorly constrained and uncontrollable variations in the experimental setup, the measurement geometry becomes an ‘unknown’ in the calibration equation and renders its solution intractable within reasonable limits of uncertainty (Weltje and Tjallingii, 2008). As a result of this uncontrollable variable in the calibration equation, the experimental setup of quantitative XRF core-scanning must incorporate control specimens of known intensities (Weltje and Tjallingii, 2008). However, such calibration approaches often possess inherent intractability which can make the exercise inappropriate for fully quantifying

core-scan ED-XRF intensities. As a result, calibration requires an alternative approach within the scope of CoDa in the form of the Log-Ratio Calibration Equation (LRCE): a univariate log-ratio calibration (ULC) approach that combines conventional calibration approaches in ratio form (Weltje et al., 2015).

The primary justification for the application of the LRCE and calibration in this study is outlined by Bloemsma (2015) in terms of deriving meaningful data. Essentially, the reason why calibration of core-scan derived XRF data is that if calibration is not performed, no actual useful information other than noise and 'presence/absence' of particular elemental data can be discerned. Calibrating the data in the manner outlined in this manuscript actually shows robustly both the relative elemental composition present, but also that the elements that are calibrated are actual signal as opposed to noise.

4. METHODOLOGY

4.1. Quantification of core-scan derived XRF through the LRCE

The LRCE works by using the relationship between elements derived from core-scan and conventional ED-XRF. Core-scan ED-XRF cannot be calibrated in standard equations due to unknown coefficients of such models, as it is not possible to correct for grain-size, water content etc., on a split core log without altering the sample. In principle, calibration of conventional ED-XRF faces the problems of being a closed dataset (i.e., appropriate data for compositional data analysis), but still representative of relative quantities of elements in a sample. However, although core-scan ED-XRF is semi-quantitative (i.e., data are in form of counts per second) there are also relative abundances of elements (i.e., core-scan ED-XRF counts are relative to the sum-total of counts that are present between

each element). If a series of points is measured using core-scan ED-XRF and subsequently sub-sampled and processed with conventional ED-XRF, then there are two datasets for the same sample: conventional ED-XRF and core-scan ED-XRF.

The two datasets that are modelled in the LRCE are the core-scan ED-XRF counts (i.e., intensity data) for which the concentration is unknown, and the concentration values (e.g., %, ppm, etc.) dataset from the same set of samples as the intensity data, that form the reference dataset in the calibration procedure. The way in which the LRCE works is that the empirical model coefficients α and β are the log-ratio equivalents of the matrix effect and detection efficiency (this is true in the case of single-element XRF spectrometry), respectively (Weltje and Tjallingii, 2008). The LRCE uses a number of independent models for the binary sub-compositions of a given set of elements to the spectrum of relative XRF intensity data by using major axis regression based on singular value decomposition (SVD) (Weltje and Tjallingii, 2008).

The LRCE can be considered a form of additive log-ratio transformation (alr) (Aitchison, 1982; 1986), whereby the transformation is performed on every linear combination of the sub-compositions examined (Weltje and Tjallingii, 2008). The key principle however is that the calibration functions in log-ratio space and that these are linear. After which, inverse log-ratio transformation and closure, the same data can be expressed in relative intensities against concentrations in binary composition (Weltje and Tjallingii, 2008). Predictions of the most optimum log-ratio denominator are allowed for in this approach which reduces any non-linearity introduced by matrix effects (Weltje and Tjallingii, 2008). Although the calibration process is carried out in log-ratio space it is possible to inverse-transform the results using the inverse-alr function, giving

208 compositional data as output (Weltje and Tjallingii, 2008; Bloemsma, 2010). The LRCE
209 derives multiple element composition estimates from XRF core-scanner output by fitting
210 a series of mutually independent models for binary sub-compositions of elements to the
211 spectrum of (relative) intensities (Weltje and Tjallingii, 2008). The variables are only
212 considered in the form of dimensionless log-ratios, which implies that normalisation prior
213 to analysis is not relevant, and this is consistent with the key tenets of the CoDa approach
214 (Weltje and Tjallingii, 2008). With this in mind, the model is unconstrained from the
215 unit-sum and non-negativity problems imposed by a closed dataset (Weltje and Tallingii,
216 2008). A full derivation of the LRCE is given in Weltje and Tjallingii (2008) and Weltje
217 et al. (2015).

218 In this study the prediction of the ED-XRF core-scan sub-composition was carried out
219 according to the following scheme:

220 • The core-scan intensity ED-XRF data and the percentage (%) concentration
221 PXRF data are examined for the α and β model parameters through major axis
222 regression by SVD (Press et al., 1994).
223 • Binary sub-compositions between intensity ED-XRF (core-scan) and %
224 concentration PXRF are plotted (i.e., the optimum log-ratio denominator that
225 gives the best linear fit is derived and a series of alr-transformations are used
226 employing this optimum log-ratio denominator, to derive a linear relationship
227 between % concentration data and intensity data).
228 • The best fit model for intensity ED-XRF – the ED-XRF data from both the %
229 concentration and predicted concentration are permuted and calculated for each
230 log-ratio pair of linear distances, which derives the best fit for the intensity ED-

XRF sub-composition (Weltje and Tjallingii, 2008). This is empirically quantified by taking the median of the squared discrepancies between the predicted and the % concentration geochemical composition with discrepancies calculated through the use of a 'leave-one-out-cross-validation' (LOOCV) (Bloemsma et al., 2012).

- The Aitchison distance between predicted and reference composition is used as the determinant for the optimal denominator element in the sub-composition (i.e., the residual variance between measurements in both the regression and predicted models) (Bloemsma et al., 2012).
- The goodness-of-fit of the optimum log-ratio denominator is derived from the residual variance and the total variance (Weltje and Tjallingii, 2008).
- The relative abundance of each element in the sub-composition from the predicted weights is determined through an inverse alr-transformation, with data expressed in a conventional (closed) form (Weltje and Tjallingii, 2008).

Data from core-scan derived ED-XRF are now calculated based on the relative abundances of the sub-composition. However, to perform any further statistical analysis of the data, they are required to be subjected to further log-ratio transformation (e.g., alr-, centred log-ratio (clr), or isometric log-ratio (ilr) transformation). As the LRCE is founded on the CoDa principles, the use of a common log-ratio denominator is unrestricted and functions as a normalisation approach (Weltje and Tjallingii, 2008). The use of a common log-ratio denominator in the calibration model is generally independent of any environmental or sedimentological considerations (i.e., the log-ratio denominator is independent of any physical reasoning for use in the calibration model) (Weltje and Tjallingii, 2008).

4.3 Joint geochemical and grain-size modelling

Grain-size and geochemical composition of clastic sediments have been found to be highly correlated as a result of the processes that control the generation of sediment from crystalline rocks (Bloemsma et al., 2012). The composition of modern sediments and their grain-size variation is due to four key factors: (i) contributions of mineralogically and texturally distinct grains from a number of divergent sources (ii) rock fragments being mechanically weathered into a finer composition, (iii) labile grains being more susceptible to chemical weathering and (iv) transport associated sorting of compositionally distinct grains (Whitmore et al., 2004).

Bloemsma et al. (2012) have expanded on this relationship between geochemical and modal grain-size variation, as geochemical variation is generally considered to reflect the pervading environmental conditions of sediment genesis. In terms of relating grain-size variation to bulk geochemical composition, it may be postulated in terms of the chemical weathering of crystalline rocks, in which the release of unstable elements as solutes takes place, whereas elements such as Al remain in the solid phase (Nesbitt and Young, 1984; Bloemsma et al., 2012).

The development of the PLS modelling approach for joint geochemical and grain-size relationships is premised on whether in a series of sediment samples derived from a source area that, over time the extent of chemical weathering was static, then the bulk geochemical variation may be attributed to; selective entrainment, transport, and deposition (Bloemsma et al., 2012). In a sedimentological context, such a one-to-one relationship between grain-size and geochemistry is rare with geochemical variability being a function of: chemical weathering; hydraulic/aerodynamic sorting; mixing; and

277 diagenesis (Bloemsma et al., 2012). In these regards, the variability between grain-size
278 and geochemistry is considered as being what is shared and what is unshared, in which
279 case if the former is removed from the data and the residuals calculated, then unknown
280 trends such as provenance may be distinguished as a result (Bloemsma et al., 2012).

281 The partial least squares (PLS) modelling approach was developed by Bloemsma
282 et al. (2012) and has two key assumptions: (1) that there is a monotonic relationship
283 between grain-size and geochemical composition, and; (2) grain-size distributions and
284 geochemical compositions are both compositional in nature, necessitating the use of
285 models in log-ratio space (Bloemsma et al., 2012).

286 Effectively, geochemical data are considered to contain two parts, with one part
287 that is correlated with grain-size, and a second part which varies independently from
288 grain-size (Bloemsma et al., 2012). The model is carried out by finding a basis for which
289 maximizes the geochemical variance explained by the grain-size (Bloemsma et al., 2012).
290 If then, the mean is subtracted from these geochemical and grain-size data matrices, the
291 values of the residuals are provided (Bloemsma et al., 2012). If there is significantly high
292 correlation found in the projection of both datasets onto the basis vectors, then these are
293 considered to be the 'shared signals' (Bloemsma et al., 2012). The residual signal is then
294 calculated by subtraction of the shared signals from the raw data, giving the variability
295 unique to each dataset (Bloemsma et al., 2012). Taking Fig. 3 for example where X\Y
296 could be considered to represent grain-size variability and Y\X representative of
297 geochemical variability, the variability shared by both data sets is indicated by X∩Y,
298 which is highlighted in grey (Bloemsma et al., 2012). In contrast to this shared
299 variability, the variability that is then unique to the geochemical data that potentially

holds relevant signals (e.g., provenance) is shown by Y\X, representing the residual geochemical variability (Bloemsma et al., 2012).

The implementation of the PLS modelling approach follows on from the work of Bloemsma et al. (2012) in which:

- clr-transformation of both the grain-size and geochemical data.
- Derive the basis Q (i.e., clr-transformed geochemical solution space) in $\mathbb{R}^D$ that can maximise the geochemical variance explained by the grain size through the Partial Least Squares (PLS) (Wold et al., 1982).
- Fit a model onto data matrices X^* (where X = L grain size classes) and Y^* (where Y = D variables).
- Subtract the mean from the X^* and Y^* to derive X_c^* and Y_c^* through the SIMPLS algorithm (de Jong, 1993) and calculate the PLS matrix decomposition.
- Orthogonalise the bases (i.e., the loadings) through SVD with the score matrices recalculated.
- Test the significance of correlation between geochemistry and grain-size distribution scores on the k-th basis vector using the Kendall and Stuart (1973) test.
- Derive *r* for any order of k, where *r* is the Pearson's correlation coefficient between the k-th column and the previously orthogonalised bases.
- With a confidence level of α and $p = 1- \alpha$, the first k of shared signals is removed if for the k the Kendall and Stuart (1973) criterion is established.

- The model is applied to all grain-size and geochemical data as the transpose of the bases are orthonormal, thus the scores of all observed grain-size distributions and geochemical compositions may then be derived by the matrix product.
- Reduced-rank approximation is used to derive the shared signal in both the grain-size and geochemistry datasets.
- Residuals calculated and subtracted from the common variability for both the GSDs and geochemistry input data.
- Mean added, such that the residual signals centre around the mean of their corresponding raw data matrix (Bloemsma et al., 2012).

Through this algorithm implementation it may be possible to derive the grain-size dependent and independent geochemical components from the dataset. The reader is referred to Bloemsma (2010), Bloemsma et al. (2012), and Bloemsma (2015) publications for a more exhaustive discussion on the PLS algorithm. However, it is only through utilising the calibrated geochemical data presented here that proxy information for environmental change may be derived, in this case for grain-size variability and the depositional environment for the Dhanchi Island site. Grain-size data was gathered from the Dhanchi Island core samples prior to PXRF analysis, following the methodology of Flood et al. (2015).

4.3. Data acquisition: Grain-size analysis

GSDs were analysed following Flood et al. (2015) using a MalvernMastersizer 2000 instrument. Data were aggregated into quarter phi intervals (φ scale) over the range of 0.02 – 2000 μm, following collection of measurements from the instrument. The centred

log-ratio transformation (clr-transformation) was implemented on all grain-size classes with any zero-valued bins of quarter phi intervals removed (i.e., where entire column vectors consisted of 0 row values). Classes of the grain-size distribution containing a zero in any of the observations (i.e., columns where only some of the row values are > 0), were amalgamated and the arithmetic mean calculated (cf. Bloemsma et al., 2012). This process was carried out on the 62.50 μm to 2000 μm fraction (i.e., 4.00 φ to –1.00 φ) for the Dhanchi Island GSD data.

4.3. Data acquisition: ITRAX™ core-scanning

Coring was carried out at Dhanchi, Bonnie Camp, and Sajnekhali in November 2011 (sites shown in Fig. 2). Three cores (one from each site) were extracted using a motor driven percussion coring device. These cores were analysed using the ITRAX™ core-scanner (Cox Analytical Systems, Mölndal, Sweden) housed at the School of Geography, University College Dublin. This is a non-destructive analytical approach which provides ED-XRF elemental profiles along with optical imagery and micro-density (X-radiography) information (Croudace et al., 2006). The geochemical data were acquired through an ED-XRF spectrometer consisting of a molybdenum cathode (Croudace et al., 2006). The voltage and current of the X-ray source was the 3kW Mo tube set to 30 kV and 50 mA respectively, with a measurement step-size of 300 μm and exposure time of 16 seconds. The latter setting was employed for expedience, to provide high-resolution scanning of all the cores (c. 25 m of material length). The element data (table of elements shown in Table 1) were processed using fitting procedures in the Q-Spec spectral analysis package in order to extract the individual elemental intensities from the spectra output

(Croudace et al., 2006). Operation of the software involved selecting elements to be extracted from the XRF spectra, with any spurious or unnecessary elemental choices or incorrect fitting parameters adjusted post hoc through a batch-controlled post-processing of the spectra (Croudace et al., 2006). Invalid readings were noted and not employed in any post-hoc processing (i.e., invalid readings were not used in the LRCE). The scan-lengths from each of the cores were 666 cm for Dhanchi-2 (hole-depth of 728 cm), 923.2 cm for Bonnie Camp (hole-depth of 1022 cm), and 639.4 cm for Sajnekhali Island (hole-depth of 791 cm). The total number of readings from each core were Dhanchi-2 with n = 22,129 valid readings from a total output of 22,201 readings (72 invalid readings), Bonnie Camp with n = 30,517 valid readings from a total output of 30,773 readings (256 invalid readings), and Sajnekhali with n = 23,822 valid readings from a total output of 24,201 (379 invalid readings).

The LRCE was applied to the global discrete sampling dataset collected (n=568) with the model then unfolded onto the elemental data from the high-resolution ITRAX™ ED-XRF (n=76,468). The alpha (α) and beta (β) slope and intercept regression parameters derived from the LRCE were used to predict the relative concentration of a sub-composition of elements (see section 5 results of this study), for this higher resolution dataset.

4.4. Data acquisition for calibration: portable X-ray fluorescence spectrometry of reference samples

Data acquisition using ED-XRF was undertaken using a Bruker S1 TURBO SD portable X-ray fluorescence (PXRF) spectrometer (Bruker Corporation, Massachusetts, USA)

consisting of a 10 mm X-Flash® SDD Peltier-cooled detector with a 4-watt (W) X-ray tube consisting of an Ag target and a maximum voltage of 40kV. Analysis was carried out on discrete samples collected from the Dhanchi-2, Bonnie Camp and Sajnekhali Island cores. In order to ascertain major and trace element composition, the elemental suite was generated using two analytical settings for each sample analysed. Major elements were acquired using a vacuum-pumped, low-energy and high current setting of 15kV and 55μA instrument setting with no filter. The vacuum-pump was used to remove air from between the sampling window and the detector and allowed for improved analysis of the material, in particular increased sensitivity to light major elements, below and including iron (Fe). The other analytical setting was used for trace element analysis and acquired without a vacuum-pump and employed a yellow filter (Ti and Al), high-energy instrument setting of 40kV and 19.60μA. With these instrument settings, elemental data are acquired for heavier elements with little sensitivity for those elements below calcium (Ca). The filter used consists of a 0.001" Ti and 0.012" Al and is already present in the instrument. Using the portable XRF, high and low energy data were acquired for each sample. Unknown samples from the Sundarbans were each measured for 16 seconds, with a set of 22 international geochemical reference standards (shown in Table 1) measured for 120 seconds, this was carried out so as to develop a robust calibration line for the PXRF instrument specific calibration. Since the Bruker software is proprietary, a full disclosure and discussion of the calibration routine is not possible in this study (cf. Rowe et al., 2012).

The calibration models used in this research depend on the estimation of error of the covariance matrices, where the magnitude of the uncertainty in the measured

413 variables is accounted for (Bloemsma 2015; Weltje et al., 2015). With this in mind, due
414 to lack of *a priori* knowledge concerning these uncertainties, replicated analysis is
415 required in order to estimate these uncertainties (Bloemsma 2015). Repeated
416 measurements were carried out on a total of 9 samples (3 per core) with 30 additional
417 measurements on each of these samples (n = 270 repeated measurements in total) using
418 the portable ED-XRF.
419
420 4.5. Data acquisition – portable ED-XRF spectra calibration
421 The raw spectra obtained from the Bruker S1 TURBO SD portable ED-XRF require a
422 calibration to convert the data into quantitative weight percentages. The calibration for
423 the portable ED-XRF unit is matrix-specific, so a calibration for major and trace elements
424 of sediments and soils was developed using a suite of 22 reference materials. The
425 calibration of the ED-XRF spectra was carried out using the Bruker AXS calibration
426 software S1CalProcess Version 2.2.32 with the reference concentrations for the low and
427 high energy calibrations produced for each element being evaluated against the
428 concentration of the element as derived from the slope and baseline corrected peak
429 heights. Linear regression analysis of the elemental concentrations quoted by the
430 manufacturers for the international geochemical reference standards are examined along
431 with elemental composition derived from the Bruker AXS S1CalProcess.
432
433 **5. RESULTS**
434 The results presented in this section reflect the data processing and outline how the LRCE
435 was applied to the integrated core-scan ED-XRF data along with the discrete samples

436 analyzed using conventional ED-XRF and grain-size analysis. The LRCE model depends
437 on comparability of the intensity measured elemental composition (i.e., data from the
438 core-scan ITRAX™ data) along with the % elemental composition (i.e., conventional
439 XRF data) a sub-composition of the elements were examined for these modelling
440 purposes.

441 The LRCE model was applied to all of the integrated core-scan samples from the
442 cores. These input data consisted of the total sample population from the three cores
443 (Dhanchi, n = 163; Bonnie Camp, n = 228; Sajnekhali, n = 176; with a total sample
444 population, n = 567) with fifteen outliers removed. These outliers were removed as they
445 deviated substantially from the general spread of data points and would bias the
446 prediction of the model. Fig. 4 shows the cross plot of results from the closed, inverse
447 transformed sub-composition of elements with calcium (Ca), iron (Fe), and potassium
448 (K) depicted in the top row (a-c) and rubidium (Rb), titanium (Ti), and zirconium (Zr)
449 shown in the bottom row (d-f). The conventional weighted (reference) ED-XRF
450 composition is on the x-axis with the integrated ITRAX™ derived intensity (predicted)
451 ED-XRF on the y-axis.

452 The lack of a full suite of elemental output is due to the fact that the majority of
453 these elements correspond to the lower energy, and thus atomically lighter, end of the
454 spectrum with poorer excitation efficiency and detection. Data derived from these lighter
455 elements are more difficult to calibrate as there tend to be more peak-overlaps. Finally, as
456 the penetration depth of ED-XRF for the light elements (e.g., Si, Al etc.,) tends to be ~
457 hundreds of μm, there is a risk of not actually measuring sediment (i.e., with core scan
458 derived ED-XRF, it is possible to measure water pooled under the Mylar® polyester

459 film). The efficacy of the LRCE is illustrated in Fig. 4, where data appears to be well
460 spread along the model, with calcium, iron and titanium representing the best spread of
461 data points. There appears to be some bias in the potassium modelled output where a
462 number of sample points deviate from the model. This bias may be attributed to the
463 measurement of potassium in ED-XRF (both core-scan and conventionally derived ED-
464 XRF), where potassium appears close to calcium and in some cases there may be some
465 peak overlap if the count time is low (Bloemsma 2015). However, given that the
466 potassium is spread along the x-axis of the known weighted elemental composition, such
467 an artefact of analysis may be attributed to the conventional ED-XRF. Rubidium data
468 points appear to be spread across the regression and derive a reduced correlation. There is
469 also a clustering of the data points from the regression model applied to zirconium.

470 The calibration coefficients, α and β, for the LRCE model are shown in Table 2
471 and Table 3, respectively. These coefficients can be considered to reflect the matrix effect
472 (i.e., scattering, absorption and enhancement effects introduced during measurement,
473 caused by the presence of other elements) and detection efficiency (i.e., sensitivity of the
474 ED-XRF data after pre-processing) in a single-element from ED-XRF derived output
475 (Weltje and Tjallingii, 2008). The LRCE removes the specimen effects, which relate to
476 the deviations of measurement from ideal conditions, however not all of these effects are
477 fully removed (Weltje and Tjallingii, 2008). The α and β regression parameters reflect
478 physical parameters such as grain-size, core-surface elevation, and water content (Weltje
479 and Tjallingii, 2008), and are the main criteria used in the LRCE for calculating the best
480 model fit for each of the elements (i.e., what is the 'best' log-ratio denominator for each
481 of the elements in the dataset) (Weltje and Tjallingii, 2008).

In Table 4 and Table 5 the residual variances of the regression and prediction of the dataset used in the LRCE are shown. The residual variance refers to noise as it does not correlate with the compositional variations in a specimen (Bloemsma, 2010). This variance is quantified by taking a clr-transformation of a set of measurements from the same core-locations (i.e., replicate measurements) with the Euclidean distance between the observations measured in order to calculate error estimation (Bloemsma, 2010). Thus, the residual variance effectively quantifies the level of relative 'noise' that may be derived from the regression and prediction. The residual variance for both the regression and prediction reveal that calcium accounts for the most consistent variance.

The α and β parameters from the log-ratio transformed dataset shown in Fig. 5 (a-e) with Ca found to be the best fitting denominator for Fe, K, Rb, Ti, and Zr. The R^2 values of goodness-of-fit in the LRCE denominator are shown in Table 6. The non-linearity found in the original back-transformed data (Fig. 5, Rb and Zr) along with bias (Fig. 5, K) is now removed. Ca is found to be the optimal denominator using the Aitchison distance between the predicted and reference composition. Table 4 shows the median variances and Table 5 depicts the 95% confidence limits corresponding to these residual variances. The non-linearity introduced by the matrix effects has been greatly reduced with log-ratio intensities now distributed linearly with the log-ratio relative concentration (cf. Weltje and Tjallingii, 2008). As a consequence, the elemental concentration can now be derived from any of the intensity observations based on the linear model (black line intersecting the point clouds in Fig. 5) (cf. Weltje and Tjallingii, 2008).

Using the residual variance of the prediction and the regression (Table 4 and Table 5), the sub-composition closure of the high-resolution dataset from the ITRAX™ ED-XRF has been estimated from the lower resolution calibration dataset. As a result, it is now possible, through the calibrated intensity derived ED-XRF with the weighted ED-XRF, to interpolate the high resolution intensity ED-XRF.

Shown in Fig. 6a is the PLS model output for the Dhanchi Island core with the PLS-coefficients of c. 0.3 for grain-size depicted by negative values corresponding to the coarse-clay to coarse-silt size fractions. Positive PLS coefficients of c. +0.3 are indicated by coarse-silt to sand sized. The PLS-scores for grain-size indicate positive score fluctuations appear to correspond to coarser sediment coefficients with negative scores found to correspond to that of finer sediment coefficients. The PLS-coefficients for geochemistry (Fig. 6b) show positive values for zirconium and calcium, with the highest negative values found for iron, potassium, rubidium, and titanium. Calcium and zirconium indicate the highest PLS coefficients at c. 0.4 and 0.3 respectively. In contrast, iron, potassium, rubidium and titanium are negatively correlated with PLS-coefficient values of between -0.3 and -0.4. The PLS-scores show a decline in grain-size with a concomitant decline in PLS-scores for geochemistry (calcium and zirconium) (Fig. 6c & d). Furthermore there is an apparent trend found in the PLS-scores for grain-size, firstly a trend consisting of a form of oscillation taking place from c. 787 cm to 491 cm that is superseded by a second trend of PLS-score decline. These trends in light of the PLS-scores may be interpreted as a form of grain-size variability, in which oscillations in grain-size appear to correlate with oscillation in zirconium, while a decline in zirconium is reflected in a decline in grain-size. When the PLS-data are considered along with the

PC1-scores and PC1-coefficients for residual geochemistry (Fig. 6e & f), it is evident that throughout the Dhanchi Island core there is a consistent decline of calcium taking place. This can be discerned through the PC1-coefficients for residual geochemistry which depict positive values driven most strongly by calcium at c. 0.7 with negative values being concomitantly driven by zirconium at just over -0.6. Furthermore, negative PC1-coefficient values may be discerned for the rubidium and titanium compositions, with potassium and iron represented by positive coefficient values.

6. DISCUSSION

6.1 Reconstructing Late Holocene environmental change from sediments in the West Bengal Sundarbans, India

The objective of the study is to investigate how the application of LRCE & PLS to Holocene sediments of a Delta environment can improve interpretation of geochemical indicators of grain-size variability. The geochemistry derived from the application of the LRCE to Holocene sediments in the present study illustrates the efficacy of these subset of elements as useful indicators of environmental change. The LRCE shows that, in the case of the Sundarbans, K, Rb, Fe, Ti, Zr, and Ca can be calibrated, with Ca found to be the best-fit denominator. The utility of these elements for interpreting environmental change within the Sundarbans can be explored by examining the Dhanchi Island core and how these calibrated data may be employed in order to interpret the depositional environment through grain-size variability. However, in order to understand the data generated in this study, there is a requirement to place into the context the key aspects of deltaic environments and how these aid in the interpretation of facies variability derived

550 through the LRCE & PLS models for the case study of the Dhanchi Island core. The role
551 of this discussion is to outline a potential set of circumstances that may characterise a
552 depositional model for this particular site in the Sundarbans.
553
554 6.2 Use of Sundarbans elemental log-ratios as environmental proxies
555 River deltas develop as coastal 'protuberances' as a result of high sediment availability
556 with variability in ocean hydrodynamics and localised coastal progradation (cf. Elliott,
557 1986; Wright, 1978; Hanebuth et al. 2012). A dynamic relationship exists in terms of
558 laterally graded intensity between sediment discharge along defined channels
559 counterbalanced with the influence of tides, waves and longshore currents (Hanebuth et
560 al., 2012). Differentiation of external forces in this manner leads to more diverse
561 organisation of deltaic environments that are more locally segmented and temporally
562 complex (Hanebuth et al., 2012). This study attempts to apply this approach to
563 considering the Sundarbans in this manner of localised variability in terms of sedimentary
564 deposition as opposed to applying a generalised model over the entirety of the Ganges-
565 Brahmaputra delta. Modern Holocene delta development is understood to have
566 commenced between 9 and 7.5 cal ka BP associated with the deceleration of sea-level
567 rise (Stanley and Warne, 1994). In terms of sediment supply, it has been found that the
568 occurrence of coastal-shelf deposits, are indicative of the provenance of sediment (Gao
569 and Collins, 2014). If the supply of sediment is 'small', then the seabed may consist only
570 of bedrock, relict sediment or reworked materials, this is known as "sediment starved"
571 (Gao and Collins, 2014, pp. 270). Conversely, thick Holocene deposits covering a large
572 area are indicative of an abundant supply of sediment (Gao and Collins, 2014). Sediment

supply is principally provided by rivers, and dependent on geographical variability at the global scale (Milliman and Farnsworth, 2011). Grain-size compositions examined with an experimental microdelta by Endo et al. (1996) have found that these compositions are strongly controlled by the textural composition of source sand, analogous to a real-world river system. These results indicate that textural composition of a depositional system is primarily determined by the textural composition of sediment input (Swift et al., 1971; Liu et al., 2000). With this the observed grain-size variability are a result of the transport and deposition processes of sediment delivery to a system, with subsequent reworking of sediments already deposited (Liu et al., 2000). Thus, the nature and amount of sediment input can therefore determine the textural characteristics of a depositional system in receipt of these sediments (Liu et al., 2000). It is now possible to fully consider the data from the Dhanchi Island core and what may be gleaned from the geochemical and grain size variability found and how these fit into the present understanding of deltaic environments.

The calcium variability in the Dhanchi Island sediments may therefore be understood as declining from a depth of approximately 500 cm to the core surface. This decline in calcium with the subsequent increase in zirconium, titanium, potassium, and rubidium composition may be interpreted as terrestrial sediment flux with diminished marine deposition. This calcium signal is pervasive in the four log-ratio pairs and does not appear to lend to the interpretation of grain size variability per se in the depositional characteristics of the Dhanchi Island site. It may be discernible that terrestrial sediment flux appears to be uncorrelated with calcium, thus, sediment provenance for the fine and coarse sediment appears to be independent of a marine or a tidally driven source.

In this context, the Dhanchi Island sediments exhibit a predisposition to terrigenous sediments, in agreement with Rogers et al. (2013) that geographical distance is not necessarily a limiting factor on sedimentation taking place (assuming the predominance of terrigenous sediment in the Dhanchi Island sediments). One of the key trends in all of these log-ratio pairs with calcium as the denominator, is that there appears to be a non-stationarity signal present, in which although the variability between log-ratio values appears to indicate some form of oscillation throughout the sequence, in each log-ratio pair however the overall behaviour as noted is an increase in the numerator value at the expense of the calcium denominator (Fig. 7). Non-stationary signals, in the case of these log-ratio pairs, implies that the depositional processes taking place are drifting in time, in particular the increase in zirconium relative to calcium may be derived from the aggradation of the island surface.

Grain size variation delivered by rivers has also been found to become finer in the seaward direction and this is more pronounced in an aggradational environment (Dalrymple and Choi, 2007). However, given that this part of the Sundarbans is an ‘abandoned’ deltaic-estuarine site, it may be classed as being part of the ‘middle estuary’ which occupies effectively the same environmental location within an estuary as active delta-plain distributary channels within a delta (Dalrymple and Choi, 2007). In terms of a deltaic system such an abandoned set of distributary channels are thought of as estuarine due to the fact that they do not carry as much river discharge and also experience reworking by tidal currents (Dalrymple, 2006; Dalrymple and Choi, 2007). These areas experience net landward transportation of sediment from the seaward margin, which is contrast to that of active delta channels that experience a reverse (Dalrymple and Choi,

2007). It has also been noted that in terms of evidence for river action in the physical structures present, there tends to be almost no evidence for seasonality in fluvial discharge (Dalrymple and Choi, 2007). Along with this, there tends to be a case in abandoned channels of such delta plain estuaries that sediments from somewhat older distributary-mouth-bar deposits experience reworking within these systems (Dalrymple and Choi, 2007). The overarching presence of silt and clay would suggest a muddy depositional environment.

As identified by Goodbred and Saito (2011) such environments are generally made of what are termed ‘sand-mud alterations’ consisting of flaser, lenticular and wavy laminations or bedding. Furthermore, such tidal flat environments are composed of bidirectional sedimentary structures such as sand-layer stacking, cross-laminations, mud-drapes, and potentially, double mud-drapes (Goodbred and Saito, 2011). These depositional features are usually indicative of tidal depositional constraints on a sedimentary system (Goodbred and Saito, 2011). In this regard, although such sedimentary structures are difficult to discern from a discrete number of grain size samples, it is possible to elucidate such a depositional environment, potentially through high-resolution core-scanning as shown in Fig. 7. However, without having a robust chronology, it is still difficult to discern such tidal sedimentary structures. In a study of grain size characteristics of tidal-bore deposition in the Qiantang Estuary by Fan et al. (2014), GSDs are found to be composed of a principal coarse and secondary fine component. The modal size, sorting, and proportions found in these coarse and fine components are ascribed to different depositional processes on the tidal flats (Fan et al.,

641 2014). Sandy laminae were found to be well sorted compared to those of muddy laminae,
642 reflecting disparate depositional stages of waning flow and slack tides (Fan et al., 2014).

643 The dominant, upward-fining in GSDs as shown in Fig. 6 & 7 may be attributed
644 to what Dalrymple et al. (1992) refer to as 'lateral shifting of channel bedforms'. Such
645 lateral shifting leads to this trend in grain size as currents tend to be higher at greater
646 depths and weaker when over bar crests (Dalrymple et al., 1992). These fining-up
647 sequences comprising muddy tidal flats may actually cap subtidal sand ridges (Wells,
648 1995). A similar model of facies succession has been proposed by Goodbred and Saito
649 (2011), where the migration of tidal channels and creeks across tidal flats, contribute to
650 this fining up facies succession. The clay fraction elucidated from the first and second
651 principal components may represent the mud-drapes and fluid-muds which may be
652 attributed to slack water or poor water flows (cf. Wells, 1995).

653 In Marine sediments, the element profile of Ca is generally considered to reflect
654 the predominant abundance of biogenic calcite (Arz et al.,1998; Tjallingii et al., 2010).
655 There is known to be poor preservation of $CaCO_3$ in the Sundarbans progradational lower
656 delta plain sequence relative to the marsh and mangrove deposits of other deltaic systems
657 around the world (Allison et al., 2003).

658 There appears to be greater agreement found between sediment provenance
659 proposed by Rogers et al. (2013) and sediment depositional model outlined here in terms
660 of distal sediment transport from fluvial sources, reflected in the log-ratio pairs discussed.
661 The non-stationary signals found in elemental log-ratio pairs may be attributed to tidal
662 processes in the manner described by Dalrymple and Choi (2007). However, what is
663 further elucidated through the joint geochemical and grain-size analysis approach is tha

664 the Sundarbans, through the Dhanchi Island example presented in this study reflects a
665 locally segmented & temporally complex system that does not fall into a singular regime
666 classification given the complex relationship that is exhibited by tidal variability
667 (Hanebuth et al., 2012). Furthermore, although sediments may undergo reworking, what
668 has been found is a predominantly terrestrial source for sediments present in the
669 Sundarbans; this does not fit closely with the implication that the Sundarbans are
670 'sediment starved' as outlined by Gao and Collins (2014). Rather, geographically
671 (Milliman and Farnsworth, 2011) and climatically (Liu et al., 2000; Gao and Collins,
672 2014) variable processes operate in producing a complex depositional environment.
673 Sedimentary facies variability in the form of tidal processes can only be inferred in this
674 study by the diminished calcium variability found. These tidal processes do not appear to
675 operate in isolation and may be coupled to some form of monsoonal variability in the
676 manner proposed by Liu et al. (2000) for Asia and by Rogers et al. (2013) more
677 specifically applied to the Sundarbans.

678 The utility of these calibrated geochemical proxies from the Sundarbans is
679 illustrated in Fig. 7 from the Dhanchi Island core. Through plotting the log-ratio pairs
680 there appears to be some oscillating trend throughout the core, in particular with log-
681 transformed Zr and Rb (see Fig. 7). There is a steady decline in Zr nearer to the top of the
682 core (from a depth of 450 cm to the core surface). This indicates a decline in zirconium,
683 and potentially an increase in rubidium. It is only through CoDa however that such a
684 trend can be illustrated in the first place as ratios by themselves possess the undesirable
685 property of asymmetry, meaning that conclusions based on evaluation of the ratio of two
686 elements (e.g., A/B), cannot be directly translated into equivalent statements about B/A

687 (Weltje, 2012; Weltje et al., 2015). Taking this approach further, the Rb and K log-
688 transformed data shown in Fig. 7, appear to reflect the trend found in rubidium and
689 zirconium; with an oscillating trend throughout the core. However, there does not appear
690 to be any discernible increase or decrease in rubidium up core, with the log-ratio data
691 remaining somewhat unvarying.

692 The overarching trend would suggest a strong relationship between zirconium and
693 coarse grained sediment, as these sites are considered to reflect upward fining sequences
694 (e.g., Allison et al., 2003; Flood et al., 2015). In particular the trend consists of
695 coarse/very coarse-silt and sand with a concomitant relationship between coarse clay and
696 medium/coarse-silt for rubidium. Furthermore, the variability of rubidium with potassium
697 would suggest an unvarying relationship between the fine-grained sediments. This might
698 indicate that fine-grained provenance is tied to rubidium and potassium, with coarse
699 grained sediment provenance strongly linked to zirconium. Ca geochemistry (shown in
700 Fig. 6 & 7) may be linked to some external environmental control, such as sea-level or
701 tidal inundation as calcium is generally only present in liquid form in the marine
702 environment. Ca appears to correlate negatively with Zr, Ti, K, and Rb in the Dhanchi
703 Island core. This decline in Ca with concomitant increases in Zr, Ti, K, and Rb (Fig. 7)
704 may be interpreted as reflecting terrestrial derived sediment flux with diminished marine
705 or carbonate deposition (or at least a marine source of variability). Terrestrial sediment
706 flux therefore appears to be uncorrelated with Ca, implying that sediment provenance is
707 independent of a marine or tidally driven source.

708

709 **7. CONCLUSION**

Through CoDa it has been possible to calibrate core-scan derived XRF data, and produce useful elemental proxies for analysing a clastic sedimentary environment. When using the LRCE calibration model coefficients to examine such clastic sedimentary environments in the Indian Sundarbans quantified data outputs are possible, and combined with grain-size data a broader understanding of the depositional environment is possible. The lack of a full elemental suite, attributed to a poorer linear fit between weighted concentration and intensity data, does not detract from the approach to XRF core-scan calibration. The elements that have been calibrated through the LRCE in this study may be used to demonstrate provenance (e.g., Zr, Rb, Ti, etc.) and processes of sedimentation (e.g., Ca) in this area of the G-B delta. Ca has been found to be the optimum log-ratio denominator, and when examined in a log-ratio framework, it may be used to distinguish between marine-terrestrial sediment fluxes in a high-resolution XRF dataset. Grain-size variability modelled with calibrated geochemistry has shown that Zr and Rb are interpreted as robust proxies for coarse and fine sediment deposition, respectively. A potential sedimentary facies model for the Sundarbans through the PLS modelling approach allows investigators to incorporate both depositional and provenance variability. Future research should focus on building a more constrained calibration model for the G-B delta, with more sedimentary cores from different facies sequences and employing other geochemical analyses tools (e.g., ICP-OES/MS). The LRCE & PLS approaches applied in this study for calibration of sediments represent a robust application of the principles of CoDa, and it is recommended that future studies in the G-B delta and other delta environments should seek to refine core-scanning XRF and grain-size analysis in light of the approaches outlined in this study.

ACKNOWLEDGEMENTS

RPF acknowledges the support provided by a Research Studentship from the Department for Employment and Learning (Northern Ireland) and the Department of Education and Science's Higher Education Grant Scheme (ROI) provided through Laois County Council (ROI). RPF also acknowledges the School of Geography, Archaeology and Palaeoecology (GAP), Queen's University, Belfast (QUB) for the fieldwork support provided by their Soulby Research Fund. RPF acknowledges the assistance and technical support provided by Mike Dobby (formerly of Bruker Instruments UK Ltd.), John Meneely and Patricia Warke (QUB), Ciara Fleming, Clare Ní Cholmáin, and David Colgan (UCD). The authors would like to thank the three anonymous reviewers for the constructive comments and help in improving the quality of this manuscript.

Reference list

Aitchison, J., 1982. The statistical analysis of compositional data (with discussion). J. R. Stat. Soc. Ser. B 44, 139–177.

Aitchison, J., 1986. The Statistical Analysis of Compositional Data. Chapman and Hall, London. 416 pp.

Allison, M.A. 1998a. Geologic framework and environmental status of the Ganges-Brahmaputra delta. Journal of Coastal Research 14, 826–836.

Allison, M.A., 1998b. Historical changes in the Ganges-Brahmaputra delta. Journal of Coastal Research 14, 1269–1275.

754 Allison, M.A., Khan, S.R., Goodbred Jr., S.L., Kuehl, S.A., 2003. Stratigraphic evolution
755 of the late Holocene Ganges-Brahmaputra lower delta plain. Sedimentary Geology
756 155, 317–342.
757 Arz, H.W., Patzold, J., Wefer, G., 1998. Correlated millennial-scale changes in surface
758 hydrography and terrigenous sediment yield inferred from last-glacial marine
759 deposits off Northeastern Brazil. Quaternary Research 50, 157–166.
760 Bhattacharyya, S., Pethick, J., Sensarma, K. 2013. Managerial response to sea level rise
761 in the tidal estuaries of the Indian Sundarban: a geomorphological approach. In
762 Xun, W., Whittington, D. (Eds.) Water Policy Journal: Special Edition: The
763 Ganges. Basin Water Policy 15, pp. 51–74.
764 Bird, E.F.C., 1984. Coasts: an introduction to coastal geomorphology. Blackwell, Oxford,
765 320 pp.
766 Bjørlykke, K., 2010. Chapter 3 Sedimentary Geochemistry: How Sediments are
767 Produced. In Bjørlykke, K. (ed.). Petroleum geoscience: From sedimentary
768 environments to rock physics. Heidelberg, Springer, 508 pp.
769 Bloemsma, M.R. (2010) Semi-Automatic Core Characterisation based on Geochemical
770 Logging Data, Unpublished M.Sc. thesis: Delft University of Technology, The
771 Netherlands, 164 pp.
772 Bloemsma, M.R. (2015) Development of a Modelling Framework for Core Data
773 Integration using XRF Scanning, Unpublished Ph.D. thesis: Delft University of
774 Technology, The Netherlands, 229 pp.

775 Bloemsma, M.R., Zabel, M., Stuut, J.B.W., Tjallingii, R., Collins, J.A., Weltje, G.J.
776 (2012) 'Modelling the joint variability of grain-size and chemical composition in
777 sediments', Sedimentary Geology, 280, pp. 135-148.
778 Croudace, I.W., Rindby, A., Rothwell, R.G., 2006. ITRAX: description and evaluation of
779 a new multi-function X-ray core scanner. In: Rothwell, R.G. (Ed.), New
780 Techniques in Sediment Core Analysis. Special Publication, vol. 267. Geological
781 Society, London, pp. 51–63.
782 Dalrymple, R.W. and Choi, K., 2007. Morphologic and facies trends through the fluvial–
783 marine transition in tide-dominated depositional systems: a schematic framework
784 for environmental and sequence-stratigraphic interpretation. Earth-Science Reviews
785 81, 135–174.
786 Dalrymple, R.W., 2006. Incised Valleys in Time and Space: An Introduction to the
787 Volume and An Examination of the Controls on Valley Formation and Filling. In:
788 Dalrymple, R.W., Leckie, D.A., Tillman, R.W. (Eds.), Incised Valleys in Time and
789 Space. SEPM (Society for Sedimentary Geology) Special Publication 85, pp. 5–12.
790 Dalrymple, R.W., Zaitlin, B.A., and Boyd, R., 1992. Estuarine facies models: conceptual
791 basis and stratigraphic implications. Journal of Sedimentary Petrology, 1130-1146.
792 de Jong, S., 1993. SIMPLS: an alternative approach to partial least squares regression.
793 Chemometrics and Intelligent Laboratory Systems 18, 251–263.
794 De Vries, J.L., Vrebos, B.A.R., 2002. Quantification of infinitely thick specimens by
795 XRF analysis. In van Grieken, R.E., Markovicz, A.A. (Eds.), Handbook of X-Ray
796 Spectrometry, Second Edition. Marcel Dekker, New York, pp. 341–405.

797 Elliott, T., 1986. Deltas. In: Reading, H.G. (Ed.), Sedimentary Environments and Facies.
798 Blackwell Scientific, Oxford, pp. 113–154.
799 Endo, N., Masuda, F., Yokokawa, M., 1996. Grain-size distributions of sediment carried
800 by single transportation modes in an experimental microdelta system. Sed. Geol.
801 102, 297–304.
802 Fan, D.D., Tu, J.B., Shang, S., Cai, G.F., 2014. Characteristics of tidal-bore deposits and
803 facies associations in the Qiantang Estuary, China. Marine Geology, 348, 1–14.
804 Flood, R.P., Orford, J.D., McKinley, J.M., Roberson, S., 2015. Effective grain-size
805 distribution analysis for interpretation of tidal–deltaic facies: West Bengal
806 Sundarbans. Sedimentary Geology, 318, 58-74.
807 Gao, S. and Collins, M.B., 2014. Holocene sedimentary systems on continental shelves.
808 Marine Geology, 352, 268–294.
809 Goodbred Jr., S.L., Kuehl, S.A., 2000. The significance of large sediment supply, active
810 tectonism and eustasy on margin sequence development: Late Quaternary
811 stratigraphy and evolution of the Ganges-Brahmaputra delta. Sedimentary Geology
812 133, 227–248.
813 Goodbred Jr., S.L., Saito, Y., 2012. Tide-dominated deltas. In: Davis, R.A., Dalrymple,
814 R.W. (Eds.), Principles of Tidal Sedimentology. Springer Science + Business
815 Media B.V, pp. 129–149.
816 Hanebuth, T.J., Proske, U., Saito, Y., Nguyen, V.L. and Ta, T.K.O., 2012. Early growth
817 stage of a large delta—Transformation from estuarine-platform to deltaic-
818 progradational conditions (the northeastern Mekong River Delta, Vietnam).
819 Sedimentary Geology, 261, 108–119.

820 Jansen, J.H.F., Van der Gaast, S.J., Koster, B., Vaars, A.J., 1998. CORTEX, a shipboard
821 XRF scanner for element analyses in split sediment cores. Quat. Res. 151, 143–153.
822 Jenkins, R., 1999. X-Ray Fluorescence Spectroscopy, Second Edition. Wiley & Sons,
823 New York. 207 pp.
824 Kendall, M.G., Stuart, A., 1973. The Advanced Theory of Statistics, Volume 2: Inference
825 and Relationships. Griffin, London.
826 Liu, J.T., Huang, J.S., Hsu, R.T. and Chyan, J.M., 2000. The coastal depositional system
827 of a small mountainous river: a perspective from grain-size distributions. Marine
828 Geology, 165, 63-86.
829 Liu, J.T., Huang, J.-S., Hsu, R.T., Chyan, J -M., 2000. The coastal depositional system of
830 a small mountainous river: a perspective from grain-size distributions. Marine
831 Geology 165, 63–86.
832 Liu, J.T., Zarillo, G.A., 1989. Distribution of grain sizes across a transgressive shoreface.
833 Mar. Geol. 87, 121–136.
834 Liu, J.T., Zarillo, G.A., 1990. Shoreface dynamics: evidence from sediment patterns and
835 bathymetry. Mar. Geol. 94 (1/2), 37–53.
836 Milliman J D, Farnsworth K L, 2011. River discharge to the coastal ocean: a global
837 synthesis. Cambridge University Press, Cambridge, 384 pp.
838 Milliman, J.D., Syvitski, J.P.M., 1992. Geomorphic/tectonic control of sediment
839 discharge to the oceans: the importance of small mountain rivers. Journal of
840 Geology 100, 525-544.

841 Nesbitt, H.W., Young, G.M., 1984. Prediction of some weathering trends of plutonic and
842 volcanic rocks based on thermodynamic and kinetic considerations. Geochimica et
843 Cosmochimica Acta 48, 1523-1548.
844 Potts, P.J., 1987. Handbook of Silicate Rock Analysis. Blackie, Glasgow. 622 pp.
845 Press, W.H., Teukolsky, S.A., Vetterling, W.T., Flannery, B.P., 1994. Numerical Recipes
846 in FORTRAN: The Art of Scientific Computing, Second Edition. University Press,
847 Cambridge. 963 pp.
848 Ramsey, M.H., Potts, P.J., Webb, P.C., Watkins, P., Watson, J.S., Coles, B.J., 1995. An
849 objective assessment of analytical method precision: comparison of ICP-AES and
850 XRF for the analysis of silicate rocks. Chem. Geol. 124, 1–19.
851 Richter, T.O., Van der Gaast, S., Koster, B., Vaars, A., Gieles, R., De Stigter, H., De
852 Haas, H., van Weering, T.C.E., 2006. The Avaatech XRF core scanner: technical
853 description and applications to NE Atlantic sediments. In: Rothwell, R.G. (Ed.),
854 New Techniques in Sediment Core Analysis. Special Publication, vol. 267.
855 Geological Society, London, pp. 39–50.
856 Rogers, K.G., Goodbred Jr., S.L., Mondal, D.R., 2013. Monsoon sedimentation on the
857 ‘abandoned’ tide-influenced Ganges-Brahmaputra delta plain. Estuarine, Coastal
858 and Shelf Science 131, 297–309.
859 Rothwell, R.G., Hoogakker, B., Thomson, J., Croudace, I.W., Frenz, M., 2006. Turbidite
860 emplacement on the southern Balearic Abyssal Plain (western Mediterranean Sea)
861 during Marine Isotope Stages 1-3: an application of ITRAX XRF scanning of
862 sediment cores to lithostratigraphic analysis. In: Rothwell, R.G. (Ed.), New

863 Techniques in Sediment Core Analysis. Special Publication, vol. 267. Geological
864 Society, London, pp. 79–98.
865 Rowe, H., Hughes, N., Robinson, K., 2012. The quantification and application of
866 handheld energy-dispersive x-ray fluorescence (ED-XRF) in mudrock
867 chemostratigraphy and geochemistry. Chemical Geology 324–325, 122–131.
868 Ryan, P., 2014. Environmental and low temperature geochemistry. New York, John
869 Wiley & Sons, 416 pp.
870 Salminen, R. (Chief editor). Geochemical atlas of Europe. Part 1: Background
871 information, methodology and maps. EuroGeoSurveys, Espoo, Finland, 2005.
872 Stanley, D.J., Warne, A.G., 1994. Worldwide initiation of Holocene marine deltas by
873 deceleration of sea-level rise. Science 265, 228–231.
874 Swift, D.J.P., Sanford, R.B., Dill, C.E., Avignone, N.F., 1971. Textural differentiation on
875 the shore face during erosional retreat of an unconsolidated coast Cape Henry to
876 Cape Hatteras, western North Atlantic Shelf. Sedimentology 16, 221–250.
877 Syvitski, J.P.M., Peckham, S. D., Hilberman, R. D., Mulder, T., 2003. Predicting the
878 terrestrial flux of sediment to the global ocean: a planetary perspective.
879 Sedimentary Geology 162, 5–24.
880 Ta, T.K.O., Nguyen, V.L., Tateishi, M., Kobayashi, I., Saito, Y., 2005. Holocene delta
881 evolution and depositional models of the Mekong River Delta, southern Vietnam.
882 In: Giosan, L., Bhattacharya, J.P. (Eds.), River deltas — concepts, models, and
883 examples: SEPM (Society Economical Palaeontologists Mineralogists) Special
884 Publication, 83, pp. 453–466.

885 Tanabe, S., Saito, Y., Vu, Q.L., Hanebuth, T.J.J., Ngo, Q.L., 2006. Holocene evolution of
886 the Song Hong (Red River) delta system, northern Vietnam. Sedimentary Geology
887 187, 29–61.
888 Thomson, J., Croudace, I.W., Rothwell, R.G., 2006. A geochemical application of the
889 ITRAX scanner to a sediment core containing eastern Mediterranean sapropel units.
890 In: Rothwell, R.G. (Ed.), New Techniques in Sediment Core Analysis. Special
891 Publication, vol. 267. Geological Society, London, pp. 65–77.
892 Tjallingii, R., 2007. Application and quality of XRF core scanning in reconstructing late
893 Pleistocene NW African continental margin sedimentation and paleoclimate
894 variations. Unpublished PhD thesis: Fachbereich Geowissenschaften Universität
895 Bremen, Germany, 114 pp.
896 Tjallingii, R., Stattegger, K., Wetzel, A. and Van Phach, P., 2010. Infilling and flooding
897 of the Mekong River incised valley during deglacial sea-level rise. Quaternary
898 Science Reviews, 29, 1432–1444.
899 Wells, J.T., 1995. Tide-dominated estuaries and tidal rivers. Developments in
900 Sedimentology, 53, pp.179-205.
901 Weltje, G.J., 2012. Quantitative models of sediment generation and provenance: State of
902 the art and future developments. Sedimentary Geology, 280, 4-20.
903 Weltje, G.J., Bloemsma, M.R., Tjallingii, R., Heslop, D., Röhl, U., Croudace, I.W., 2015.
904 Prediction of geochemical composition from XRF-core-scanner data: A new
905 multivariate approach including automatic selection of calibration samples and
906 quantification of uncertainties. In Croudace, I.W., and Rothwell, R.G., (eds.)
907 Micro-XRF Studies of Sediment Cores: Applications of a non-destructive tool for

the environmental sciences. Dordrecht, NL, Springer, 507-534. (Developments in Paleoenvironmental Research, 17).

Weltje, G.J., Tjallingii, R., 2008. Calibration of XRF core scanners for quantitative geochemical logging of sediment cores: theory and application. Earth and Planetary Science Letters, 274(3), 423-438.

Wright, L.D., 1978. River deltas. In: Davis Jr., R.A. (Ed.), Coastal Sedimentary Environments. Springer, New York, pp. 5–68.

Wold, S., Martens, H., Wold, H., 1982. The multivariate calibration problem in chemistry solved by the PLS method. In: Ruhe, A., Kagstrom, B. (Eds.), Proc. Conf. Matrix Pencils. Springer Verlag, Heidelberg, pp. 286–293.

Yoshida, S., Steel, R.J., Dalrymple, R.W., 2007. Changes in depositional processes — an ingredient in a new generation of sequence-stratigraphic models. Journal of Sedimentary Research 77, 447–460.

List of Tables

931 Table 6: R^2 values of LRCE (Ca R^2 values highlighted in bold, representative of optimum
932 log-ratio denominator) of Sundarbans dataset
933
934 **List of Figures**
935
936 Fig. 1 Extent of the G-B tidal delta complex, (a) West Bengal Sundarbans (India), (b)
937 East Bengal Sundarbans (Bangladesh), and (c) Kuakata Peninsula (Bangladesh) (adapted
938 from Rogers et al., 2013)
939 Fig. 2 Sites cored in the West Bengal Sundarbans, India (November 2010) (after Flood et
940 al., 2015)
941 Fig. 3 Graphical representation of the rationale behind the calibration approach. Further
942 details are provided in the text (adapted from Bloemsma et al., 2012)
943 Fig. 4 Results of the calibration of the ED-XRF data, with the reference bulk composition
944 (x-axis) and predicted bulk chemistry (y-axis) of discrete samples from the Dhanchi-2,
945 Bonnie Camp, and Sajnekhali Island cores. Calcium (Ca) is shown in (a), iron (Fe) is
946 shown in (b), potassium is shown in (c), rubidium is shown in (d), titanium is shown in
947 (e), and zirconium (Zr) is shown in (f)
948 Fig. 5 Linear fit between log-ratio measured intensities and log-ratio of the reference bulk
949 chemistry with Ca as the optimum log-ratio denominator from the discrete samples of the
950 Dhanchi-2, Bonnie Camp, and Sajnekhali Island cores. Fit of iron and calcium shown in
951 (a), fit of potassium and calcium shown in (b), fit of rubidium and calcium shown in (c),
952 fit of titanium and calcium shown in (d), and fit of zirconium and calcium shown in (e)

953 Fig. 6 Partial least squares (PLS) model of grain-size and calibrated geochemistry for the

954 Dhanchi Island core

955 Fig. 7 Log-ratio elemental logs from the Dhanchi Island core

International geochemical reference standard	Alternative Reference	Origin	Issuing Body	Description	Accepted values (% concentration) for international geochemical reference standards used in the Bruker AXS S1CalProcess calibration software and subsequent LRCE.						Minimum values (following Mudrock calibration of PXRF)						Maximum values (following Mudrock calibration of PXRF)					
					K	Ca	Ti	Fe	Rb	Zr	K	Ca	Ti	Fe	Rb	Zr	K	Ca	Ti	Fe	Rb	Zr
GSD-1	GBW 07310	China IGGE IRMA	IGGE	Stream Sediment	2.770	4.600	0.980	7.350	0.116	0.310	0.514	4.174	0.567	6.396	0.114	0.324	2.628	4.523	0.870	6.681	0.127	0.334
GSD-2	GBW 07302	China	IGGE	Stream Sediment	5.190	0.250	0.230	1.890	0.470	0.460	3.064	0.405	0.128	3.046	0.477	0.434	5.469	0.438	0.281	3.122	0.510	0.461
GSD-3	GBW 07303	China	IGGE	Stream Sediment	2.460	0.220	1.060	6.510	0.079	0.220	0.689	0.276	0.842	6.194	0.085	0.205	2.626	0.350	1.091	6.878	0.087	0.245
GSD-4	GBW 07304	China	IGGE	Pond Sediment	2.230	7.520	0.890	5.900	0.130	0.188	0.559	6.792	0.522	5.583	0.130	0.178	2.260	7.260	0.828	6.129	0.137	0.195
GSD-5	GBW 07305	China	IGGE	Pond Sediment	2.100	5.340	0.900	5.860	0.118	0.220	0.739	4.937	0.570	5.482	0.115	0.198	2.248	5.386	0.832	6.133	0.120	0.211
GSD-6	GBW 07306	China	IGGE	Stream Sediment	2.440	3.870	0.780	5.880	0.107	0.170	0.745	3.628	0.434	5.590	0.116	0.192	2.425	4.007	0.700	5.915	0.122	0.204
GSD-7	GBW 07307	China	IGGE	Stream Sediment	3.550	1.660	0.750	6.490	0.147	0.162	0.738	1.589	0.484	6.355	0.142	0.157	3.523	1.743	0.764	6.644	0.155	0.178
GSD-8	GBW 07308	China IGGE IRMA	IGGE	Steam Sediment 142308	2.830	0.250	0.310	2.200	0.132	0.490	1.584	0.272	0.509	2.754	0.122	0.454	3.242	0.387	0.686	3.260	0.156	0.504
GSD-9	GBW 01309	China IGGE IRMA	IGGE	Sediment 300603	1.990	5.350	0.920	4.860	0.080	0.370	0.669	5.463	0.565	4.921	0.079	0.360	2.180	5.996	0.847	4.943	0.094	0.375
GSD-10	GBW 07310	China	IGGE	Stream Sediment	0.125	0.700	0.210	3.860	0.009	0.070	0.216	0.722	0.080	3.062	0.010	0.066	0.551	0.915	0.289	4.352	0.016	0.096
GSD-11	GBW 07311	China	IGGE	Stream Sediment	3.280	0.470	0.350	4.390	0.408	0.153	1.354	0.533	0.189	3.497	0.350	0.138	3.313	0.578	0.399	3.692	0.396	0.157
GSD-12	GBW 07312	China	IGGE	Stream Sediment	2.910	1.160	0.250	4.880	0.270	0.234	1.149	1.064	0.070	4.088	0.250	0.207	2.915	1.223	0.291	4.462	0.266	0.235
GSS-1	GBW 07401	China	IGGE	Dark Brown Soil	2.590	1.720	0.810	5.190	0.140	0.245	1.173	1.588	0.620	4.986	0.145	0.252	2.597	1.804	0.854	5.511	0.152	0.276
GSS-2	GBW 07402	China	IGGE	Chestnut Soil	2.540	2.360	0.450	3.520	0.088	0.219	1.586	1.990	0.305	3.771	0.101	0.209	2.710	2.495	0.496	3.893	0.104	0.240
GSS-3	GBW 07403	China	IGGE	Yellow Brown Soil	3.040	1.270	0.370	2.000	0.085	0.246	2.128	1.207	0.316	2.905	0.096	0.275	3.427	1.388	0.453	3.045	0.102	0.313
GSS-4	GBW 07404	China	IGGE	Limy Soil	1.030	0.260	1.800	10.300	0.075	0.500	0.094	0.255	1.568	10.848	0.055	0.418	1.365	0.351	1.874	11.194	0.075	0.463
GSS-5	GBW 07405	China	IGGE	Yellow Red Soil	1.500	0.095	1.050	12.620	0.117	0.272	*ND*	0.160	0.796	12.240	0.063	0.144	1.774	0.189	1.140	12.979	0.069	0.176
GSS-6	GBW 07406	China	IGGE	Yellow Red Soil	1.700	0.220	0.730	8.090	0.237	0.220	0.517	0.266	0.592	8.941	0.184	0.161	1.955	0.316	0.841	9.236	0.205	0.185
GSS-7	GBW 07407	China	IGGE	Laterite Soil	0.200	0.160	3.360	18.760	0.016	0.318	*ND*	0.125	2.848	17.128	0.008	0.265	0.594	0.224	3.342	18.074	0.014	0.304
GSS-8	GBW 07408	China	IGGE	Loess	2.240	8.270	0.630	4.480	0.096	0.229	0.790	7.925	0.266	4.433	0.102	0.217	2.481	8.408	0.562	4.827	0.106	0.241
JSD-1		Geological Survey of Japan	GSJ	Stream Sediment	2.190	3.070	0.650	5.110	0.065	0.000	1.002	2.769	0.469	5.274	0.077	0.158	2.283	3.063	0.687	5.283	0.084	0.177
MAG-1		U.S. Dept. of the Int. Geo. Survey	USGS-AEG	Marine mud (Gulf of Maine)	3.550	1.370	0.751	6.800	0.149	0.126	1.412	0.369	0.266	3.958	0.149	0.114	2.971	0.531	0.625	4.476	0.173	0.136

ND: No data

	Ca	Fe	K	Rb	Ti	Zr
Ca	0	0.8436	0.8486	0.9553	0.8735	0.8917
Fe	0.8436	0	1.2911	-10.2447	0.5525	0.8518
K	0.8486	1.2911	0	27.9561	6.2592	1.1371
Rb	0.9553	-10.2447	27.9561	0	42.3024	1.2566
Ti	0.8735	0.5525	6.2592	42.3024	0	1.1717
Zr	0.8918	0.8518	1.1371	1.2566	1.1717	0

	Ca	Fe	K	Rb	Ti	Zr
Ca	0	1.626	-0.4527	0.8188	0.7702	0.082
Fe	-1.626	0	-3.5275	51.179	0.1718	-1.5035
K	0.4527	3.5275	0	-37.787	-0.445	-0.0172
Rb	-0.8188	-51.179	37.787	0	46.9791	-1.0694
Ti	-0.7702	-0.1718	0.4449	-46.9791	0	-1.2133
Zr	-0.082	1.5035	0.01717	1.0694	1.2133	0

	Ca	Fe	K	Rb	Ti	Zr
Ca	0	0.00945	0.00793	0.01423	0.00697	0.01032
Fe	0.00945	0	0.00192	0.00872	0.00167	0.01209
K	0.00793	0.00192	0	0.00892	0.00119	0.00984
Rb	0.01423	0.00872	0.00892	0	0.00829	0.00914
Ti	0.00697	0.00167	0.00119	0.00829	0	0.01067
Zr	0.01032	0.01209	0.00984	0.00914	0.01067	0

	Ca	Fe	K	Rb	Ti	Zr
Ca	0	0.00951	0.00798	0.01435	0.00704	0.01044
Fe	0.00951	0	0.00194	0.00881	0.00168	0.01217
K	0.00798	0.00194	0	0.00909	0.0012	0.00987
Rb	0.01435	0.00881	0.00909	0	0.00833	0.0092
Ti	0.00704	0.00168	0.0012	0.00833	0	0.01068
Zr	0.01044	0.01217	0.00987	0.0092	0.01068	0

	Ca	Fe	K	Rb	Ti	Zr
Ca	0	0.9399	0.9602	0.9122	0.9593	0.9104
Fe	**0.9399**	0	0.5076	0.2524	0.4248	0.6758
K	**0.9602**	0.5076	0	0.3844	0.0773	0.7085
Rb	**0.9122**	0.2524	0.3844	0	0.4952	0.7768
Ti	**0.9593**	0.4248	0.0773	0.4952	0	0.6912
Zr	**0.9104**	0.6758	0.7085	0.7768	0.6912	0

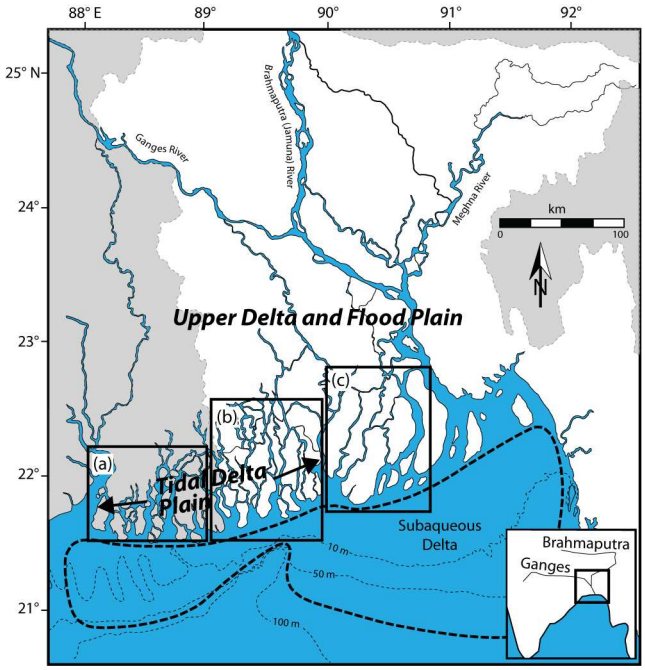

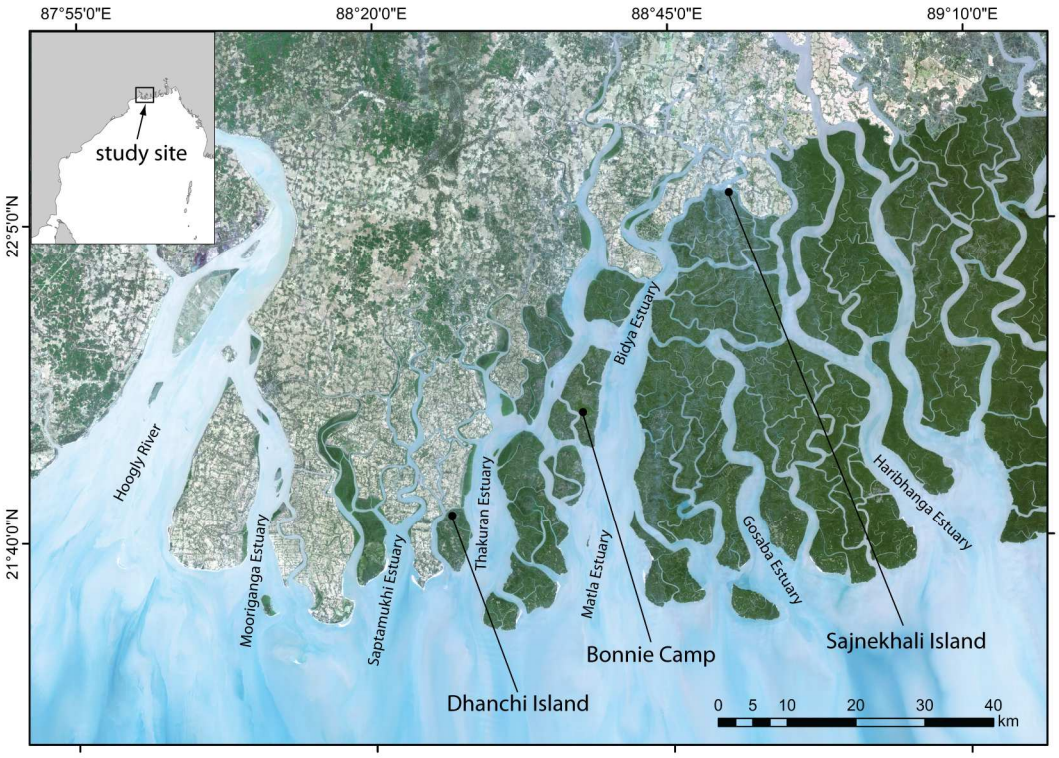

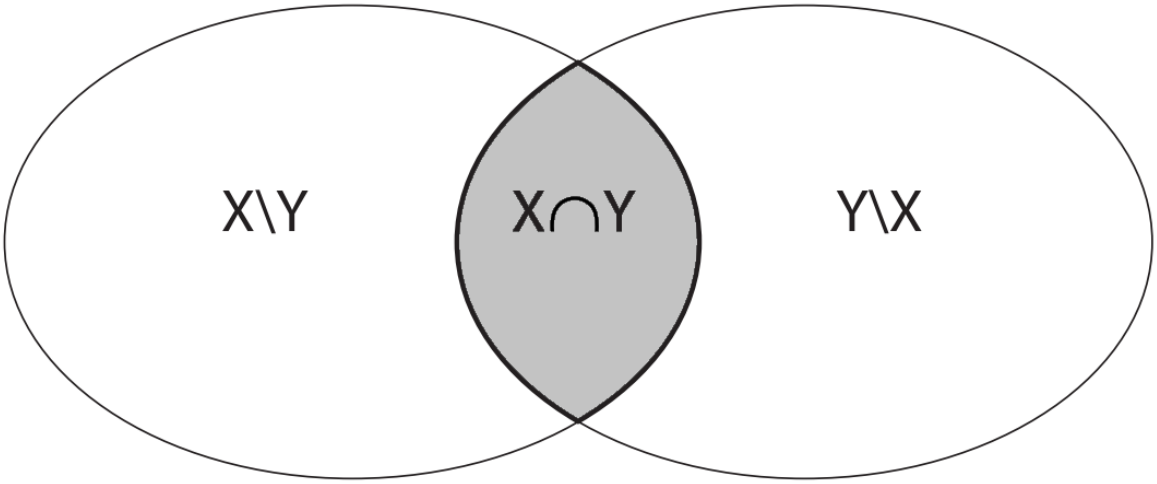

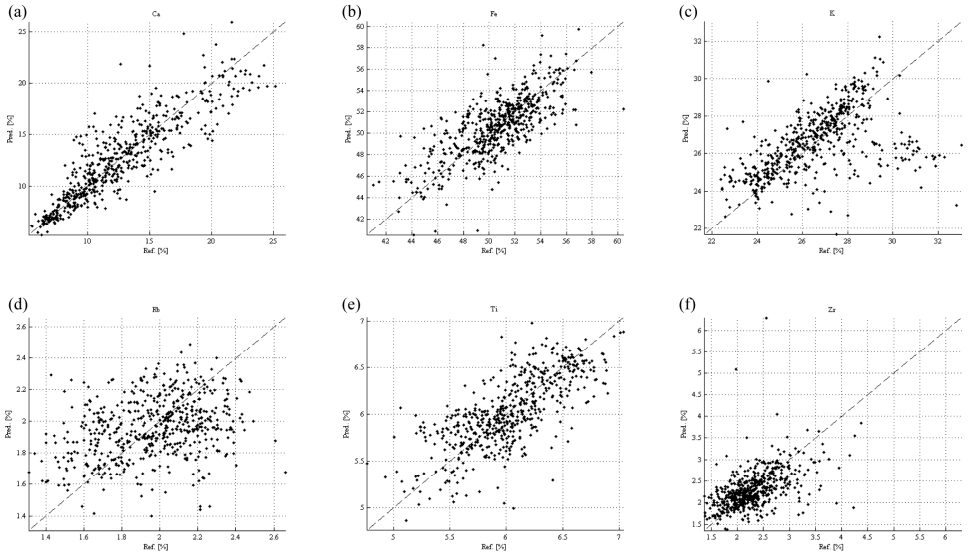

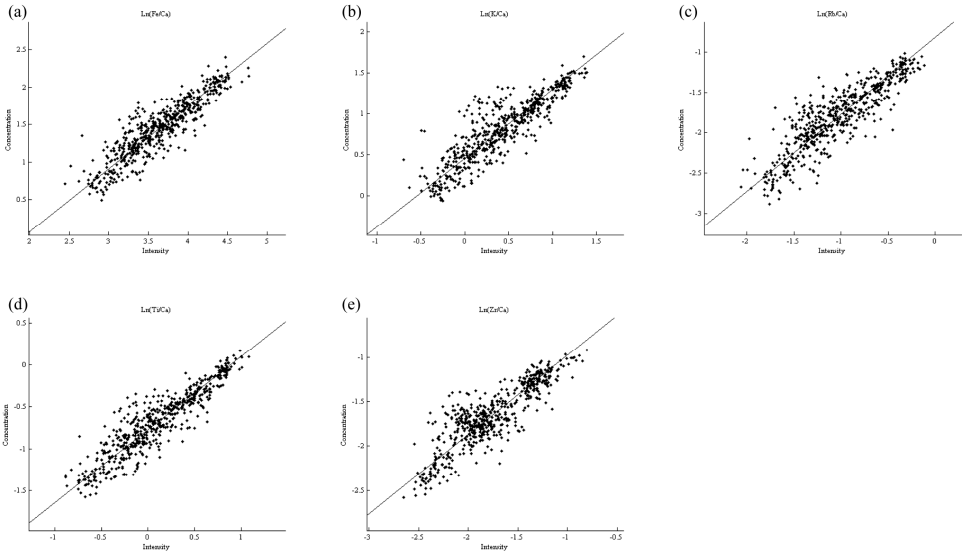

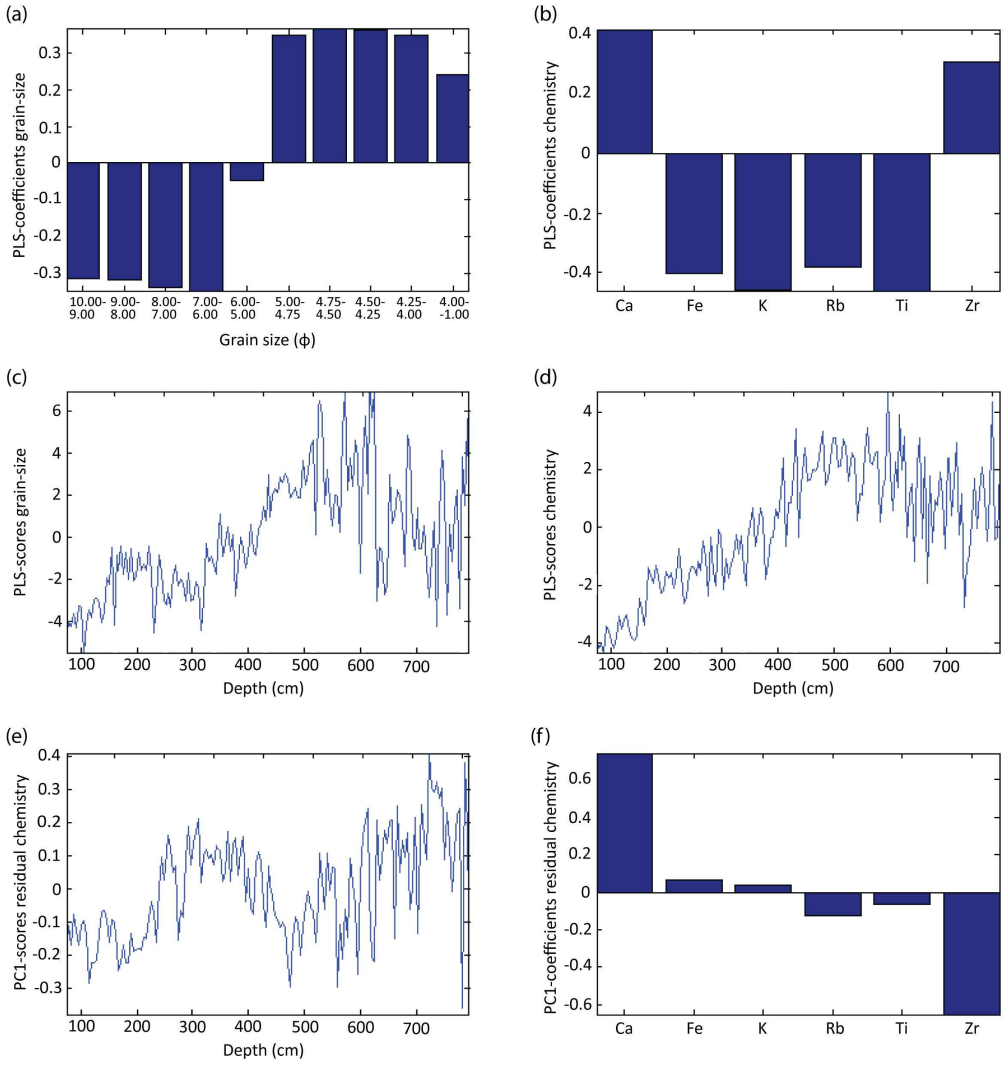
(a)
PLS-coefficients grain-size
0.3
0.2
0.1
0
-0.1
-0.2
-0.3
10.00-9.00
9.00-8.00
8.00-7.00
7.00-6.00
6.00-5.00
5.00-4.75
4.75-4.50
4.50-4.25
4.25-4.00
4.00--1.00
Grain size (ϕ)
(b)
PLS-coefficients chemistry
0.4
0.2
0
-0.2
-0.4
Ca
Fe
K
Rb
Ti
Zr
(c)
PLS-scores grain-size
6
4
2
0
-2
-4
100
200
300
400
500
600
700
Depth (cm)
(d)
PLS-scores chemistry
4
2
0
-2
-4
100
200
300
400
500
600
700
Depth (cm)
(e)
PC1-scores residual chemistry
0.4
0.3
0.2
0.1
0
-0.1
-0.2
-0.3
100
200
300
400
500
600
700
Depth (cm)
(f)
PC1-coefficients residual chemistry
0.6
0.4
0.2
0
-0.2
-0.4
-0.6
Ca
Fe
K
Rb
Ti
Zr

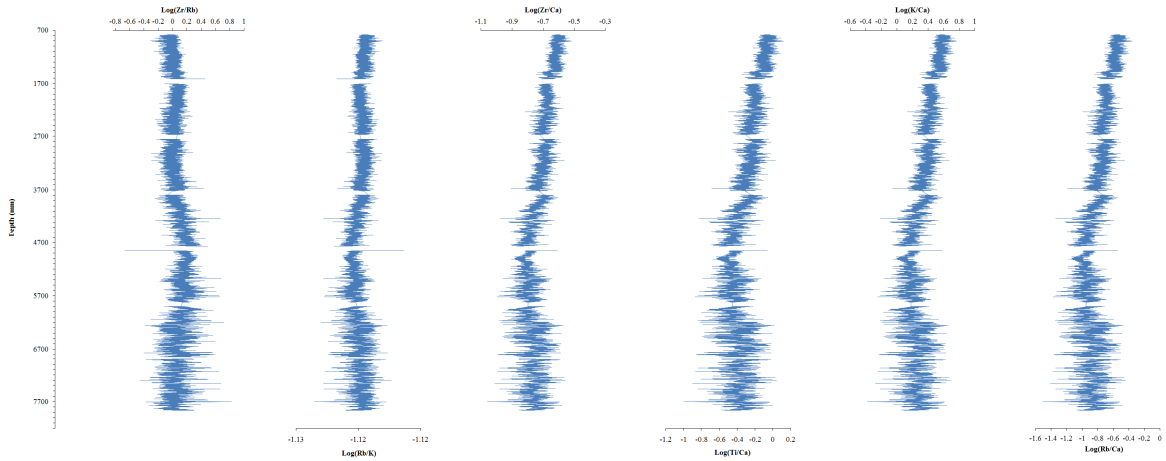

Highlights

- Multivariate statistical modelling of grain-size and geochemistry from the Holocene Ganges-Brahmaputra delta
- Compositional data analysis through log-ratio calibration and partial least squares modelling approaches for proxy depositional information
- Methodological framework for unravelling Holocene sedimentation patterns in the Ganges-Brahmaputra delta